Materials Characterization 217 (2024) 114435

Contents lists available at ScienceDirect

Materials Characterization

journal homepage: www.elsevier.com/locate/matchar

Quantitative revealing the solute segregation behavior at melt pool boundary in additively manufactured stainless steel using a novel processing method for precise positioning by HAADF-STEM

Fei Sun [a,*], Yoshitaka Adachi [a], Kazuhisa Sato [b], Takuya Ishimoto [c], Takayoshi Nakano [d,e], Yuichiro Koizumi [d,e]

[a] Department of Material Design Innovation Engineering, Nagoya University, Furo-cho, Chikusa-ku, Nagoya 464-8603, Japan
[b] Research Center for Ultra-High Voltage Electron Microscopy, Osaka University, 7-1 Mihogaoka, Osaka, Ibaraki 567-0047, Japan
[c] Aluminium Research Center, University of Toyama, 3190, Gofuku, Toyama 930-8555, Japan
[d] Division of Materials and Manufacturing Science, Graduate School of Engineering, Osaka University, 2-1 Yamadaoka, Suita, Osaka 565-0871, Japan
[e] Anisotropic Design & Additive Manufacturing Research Center, Osaka University, 2-1 Yamadaoka, Suita, Osaka 565-0871, Japan

ARTICLE INFO

Keywords:
Additive manufacturing
Melt pool boundary
Cellular structure
Segregation

ABSTRACT

Laser-powder bed fusion (LPBF) enables the fabrication of complex metallic components by manipulating various laser scan strategies to control microstructure and texture. Multiple thermal cycling and rapid solidification lead to non-equilibrium, non-uniform microstructure, and micro-segregation at the melt pool boundary (MPB), whose accurate location is still invisible by transmission electron microscopy (TEM), and quantitative concentration remains imprecise. In this study, we proposed a novel method to make it clear by controlling the crystallographic texture of 316 L stainless steel through unique LPBF processing parameters to obtain a single-crystal-like microstructure of the cellular structures along the laser scanning direction. The accurate location of the track-track MPB is distinguishable by means of the transverse and longitudinal cellular dislocation structures on both sides. The edge-on state of the track-track MPB makes the quantitative concentration analysis precisely using high-angle annular dark-field scanning TEM with energy-dispersive X-ray spectroscopy, which is in good agreement with the Scheil-Gulliver solidification simulations.

1. Introduction

Additive manufacturing (AM) has demonstrated tremendous potential for fabricating metallic components of near-net shapes with an unprecedented combination of superior properties and is gradually being adopted by the automotive and aerospace industries to produce commercially viable parts, thereby disrupting the traditional manufacturing routes [1–8]. Laser powder bed fusion (LPBF) is currently the dominant metal AM technology [9,10]. During LPBF processing, metal powders are heated and melted rapidly and periodically by a fast-moving laser beam, contributing to the complex solidification nature in the melt pool with large thermal gradients ($\sim 10^7$ K/m) and high cooling rates ($\sim 10^7$ K/s), leading to rapid solidification with high solidification growth rate ($\sim 10^{-1}$ m/s) and consequently generating non-equilibrium micro-segregation and predictable solidification microstructure according to the relationship between the thermal gradient and the solidification growth rate [3,6,7,11].

Among the LPBF-processed metallic materials, 316 L stainless steel (316LSS) is one of the extensively used materials in various engineering domains due to its excellent mechanical properties and superior corrosion resistance [12,13]. The LPBF-processed 316LSS can break the strength and ductility trade-off, which is achieved by the cellular structure with high-density dislocations and solute micro-segregation or precipitates at the cellular boundaries [14–16]. Different laser scanning strategies can change the direction of the temperature gradient within the melt pool, resulting in different morphologies and growth directions of cellular structures from the melt pool boundary (MPB) [8,17–19]. Epitaxial growth characteristics are exhibited at layer-layer MPB, while the columnar structure orientations on both sides of the track-track MPB are significantly different, proposing the possibility of identifying the precise location of the track-track MPB [20]. The maximum cooling rate located at the MPB induces the occurrence of micro-segregation, making

* Corresponding author.
E-mail address: sun.fei@material.nagoya-u.ac.jp (F. Sun).

https://doi.org/10.1016/j.matchar.2024.114435
Received 13 February 2024; Received in revised form 26 September 2024; Accepted 3 October 2024
Available online 5 October 2024

the MPB visible by optical microscopy (OM) and scanning electron microscopy (SEM) after chemical etching. The spatial resolution of energy-dispersive X-ray spectrometry (EDS) equipped with SEM limits the solute segregation behavior analysis at the MPB. Even though its precise location cannot be identified, slightly micro-segregation behavior at the approximate MPB location has been proposed that the concentrations of Cr, Mn, and Mo were lower both at the MPBs in the LPBF-processed 316LSS and within the cellular interiors as compared to cellular boundaries. With the increasing spatial resolution, the solute segregation to the MPB is possible to be detected by high resolution transmission electron microscopy (HRTEM). However, the exact location of the MPB should be identified in advance using TEM and scanning TEM (STEM) imaging, employing diffraction contrast, strain contrast, and *Z*-contrast to ensure getting credible solute segregation results [21,22].

In this study, we controlled the epitaxial growth directions of the columnar structures at both sides of the track-track MPBs by unique LPBF processing parameters, e.g. laser scan strategy, laser power, laser scan speed, hatch spacing, layer height, etc., aiming to clarify the precise location of the track-track MPB, which can be distinguishable using TEM combined with a striking contrast of different kinds of cellular dislocation structures and quantitively analyze the micro-segregation behavior at the track-track MPB. In addition, in comparison with the thermodynamic equilibrium calculation, Scheil-Gulliver solidification simulations were carried out to simulate the non-equilibrium solidification process and the solute segregation behaviors at the last stage of solidification when the most segregated liquid solidifies.

2. Experimental procedure

We employed gas-atomized 316 L SS powder with a nominal composition of Fe-18Cr-14Ni-2.5Mo-0.03C (wt%) and a particle size under 53 μm. The LPBF fabrication was performed using a 3D printer (EOSM290, EOS GmbH, Germany) equipped with a Yb-fiber laser by "X-scan strategy", as shown in Fig. 1(a), indicating the laser beam was scanned bidirectionally along the X-axis without rotation [23]. The sample was printed as cubes of 10 × 10 × 10 mm with a laser power of 250 W, a scan speed of 600 mm/s, hatch spacing of 80 μm and layer height of 40 μm. The specimens were cut from the cross-sections of the as-printed samples containing the build direction (BD), laser scan direction (SD), and transverse direction (TD) and then further polished using an automatic polishing machine (PRESI, Mecatech 250 SPI). To reveal the solidification microstructures, the polished specimens were electrochemically etched in a solution of nitric and hydrochloric acid (HNO_3:HCl:H_2O = 1:10:10). Microstructural characterization was performed on the as-built specimen without heat treatment. Microstructural features were observed by optical microscopy (OM, WRAYMER Inc., Osaka, Japan) and field emission scanning electron microscopy (FE-SEM, JSM-7001F, JEOL, Tokyo, Japan) equipped with an electron backscatter diffraction (EBSD) detector. The inverse pole figure (IPF) map was subsequently analyzed based on the EBSD results using OIM analysis software. TEM specimens were prepared using a focused ion beam (FIB) instrument (Scios2 Dual Beam, Thermo Fisher Scientific, Hillsboro, OR, USA) with Ga ions. TEM observations were conducted on JEM-2100PUS (JEOL Ltd., Tokyo, Japan) and JEM-ARM200F (JEOL Ltd., Tokyo, Japan). Compositional analysis was performed in high-angle annular dark-field scanning transmission electron microscopy (HAADF-STEM) mode using EDS attached to the 200 kV JEOL JEM-ARM200F. All the Scheil solidification calculations were performed based on the classic Scheil with fast diffusers and Scheil with back diffusion in the primary phase and fast diffusers model configurations by commercial thermodynamic software Thermo-Calc with the database of TCFE11 and MOBFE6.

3. Results and discussion

The three-dimensional visualization of the solidification microstructure of LPBF-processed 316LSS is shown in Fig. 1(b) using the OM images observed along BD, SD, and TD. The laser scan tracks formed by the X laser scan strategy are displayed obviously in the XY plane. The MPBs were distributed regularly along the BD in the YZ plane. During the LPBF processing, the rapid formation of new melt pools involves new layer-layer MPBs and overlapped track-track MPBs, suffering from local remelting of precious layers and rapid solidification. The MPBs highlighted by yellow and red solid lines indicate layer-layer MPBs and track-track MPBs, respectively. Fig. 1(c) shows the high-magnification OM image involving the minor layer along the BD in the center of the melt pools, enabling crystallographic lamellar microstructure formation in the YZ plane.

Fig. 2(a) shows the SEM image of the solidification microstructure of the major layer in the YZ plane between two adjacent minor layers along the BD, indicated by the white arrows at the upper right and lower left in the SEM image. The layer-layer MPBs and track-track MPBs are highlighted by yellow and red arrows, respectively. In each melt pool, the slender columnar structures grow epitaxially across the lay-layer MPBs along {100} orientations towards the top center of the melt pool resulting from the local thermal gradient. Fig. 2(b) shows the EBSD IPF map of the solidification microstructure in the YZ plane, indicating the side-branching columnar structures with almost a single crystal-like orientation along [001] in the major layers and polycrystalline orientations in the minor layers. The blue dashed lines on both sides of the minor layers indicate the side-branching slender columnar structures epitaxially growing from the MPBs (marked by black solid lines) along orthogonal directions. Figs. 2(c) and (d) show the TEM bright field images of the transverse and longitudinal cross-sections of columnar structures, respectively. The average size of the dislocation cells is around 500 nm. The cellular boundaries are tangled with high-density

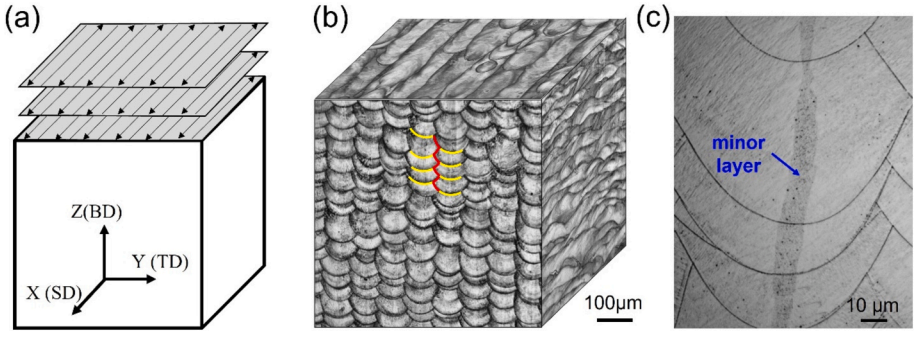

Fig. 1. (a) Schematic diagram of the LPBF process, (b) three-dimensional visualization of the solidification structure of the 316 L stainless steel fabricated by LPBF. The yellow and red lines indicate layer-layer MPB and track-track MPB, respectively, (c) minor layer exists in the center of the melt pools along the BD, forming crystallographic lamellar microstructure in the YZ plane. (For interpretation of the references to colour in this figure legend, the reader is referred to the web version of this article.)

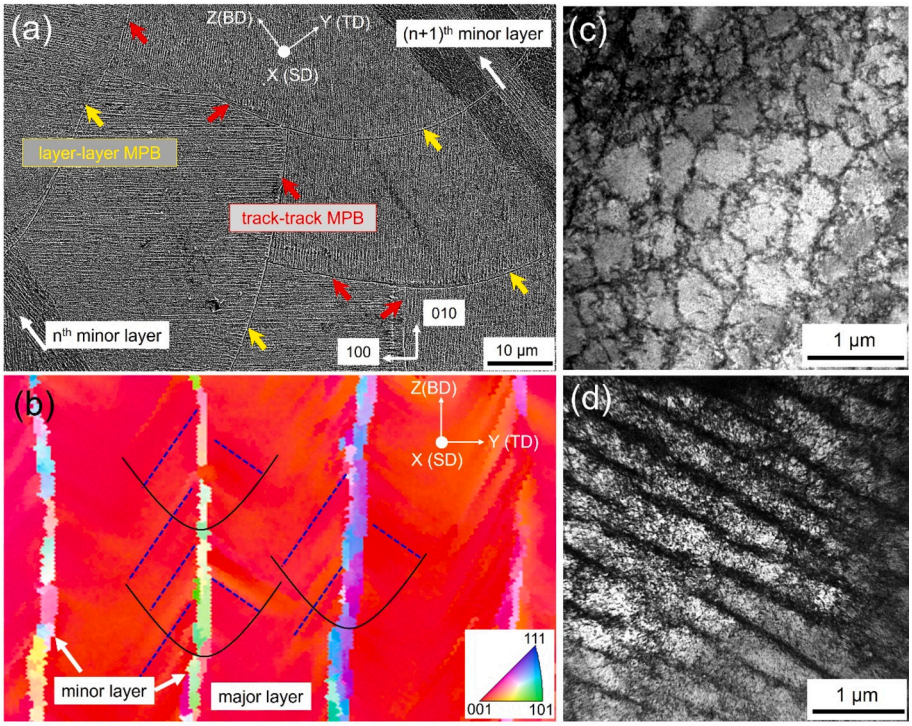

Fig. 2. (a) SEM image of the solidification microstructure of the major layer between two adjacent minor layers, including layer-layer MPB (yellow arrows) and track-track MPB (red arrows). (b) EBSD IPF micrograph of the YZ plane indicating the orientation of the columnar structures (marked by the blue dotted lines). (c) and (d) TEM bright field images of transverse and longitudinal sections of columnar structures, respectively. (For interpretation of the references to colour in this figure legend, the reader is referred to the web version of this article.)

dislocations, significantly governing the strengthening mechanism of the LPBF-processed 316LSS.

Fig. 3(a) shows the HAADF-STEM image of the microstructure near the track-track MPB. The transverse and longitudinal cross-sections of columnar structures within two adjacent melt pools can be observed. The exact location of the track-track MPB can be identified and highlighted by the red arrow for easier visualization, which has not been successfully achieved by other researchers until now. Fig. 3(b) shows the corresponding diffraction pattern of the region shown in Fig. 3(a), taken with the incident beam parallel to the [001] direction. According to the diffraction pattern, the two orientations of the columnar structures are exactly along {001} directions, consistent with the EBSD IPF map in Fig. 2(b). In addition, the single-crystal-like microstructure makes the track-track MPB in the edge-on state, which is helpful for quantitative analysis of the micro-segregation behaviors in the following. The bright contrast in the HAADF-STEM image indicates the high density of dislocations with elemental segregation. Figs. 3(c)-(j) show the corresponding EDS maps with the most remarkable contrast up to now, clearly indicating that Cr, Mn, Mo, and Ni are depleted at the MPB while Fe is enriched. On the contrary, Cr, Mn, Mo, and Ni are enriched for the

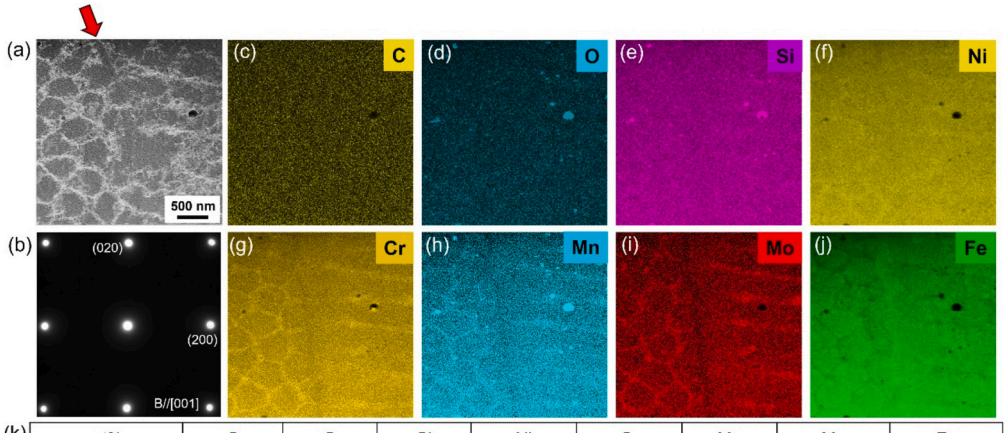

(k)

wt%	C	O	Si	Ni	Cr	Mn	Mo	Fe
MPB	0.04 ± 0.01	1.04 ± 0.27	0.32 ± 0.06	14.15 ± 0.12	16.42 ± 0.11	1.53 ± 0.15	2.52 ± 0.16	63.98 ± 0.21
Cellular boundary	0.03 ± 0.01	0.65 ± 0.18	0.34 ± 0.01	14.59 ± 0.15	17.67 ± 0.17	1.79 ± 0.13	4.03 ± 0.11	60.9 ± 0.14
Cellular interior	0.04 ± 0.01	0.82 ± 0.13	0.31 ± 0.01	14.44 ± 0.13	16.99 ± 0.16	1.63 ± 0.14	3.22 ± 0.15	62.55 ± 0.18

Fig. 3. (a) HAADF-STEM image of the track-track MPB in YZ plane, (b) the corresponding diffraction pattern with zone axis [001], (c)-(j) STEM-EDS mappings of C, O, Si, Ni, Cr, Mn, Mo and Fe, respectively, (k) element concentration at MPB, cellular boundary and interiors.

cellular boundaries, while Fe is depleted. In addition, some black particles shown in the HAADF-STEM image show oxide inclusion enriched by O, Mn, and Si. Similar oxide inclusions have commonly been reported in AM austenitic stainless steels with tens of nanometers and a few microns. Fig. 3(k) lists the quantitative concentration at the track-track MPB, cellular boundaries, and interiors. Compared with the concentration in the cellular interiors, the Cr and Mo elements were slightly depleted by 0.5–0.7 wt% at the MPB while enriched by 0.6–0.8 wt% at the cellular boundary. The Mn and Ni elements were slightly depleted by 0.1–0.3 wt% at the MPB while slightly enriched by 0.1–0.2 wt% at the cellular boundary. The Fe element was enriched by 1.5 wt% at the MPB while depleted by 1.5 wt% at the cellular boundary.

Fig. 4(a)-(c) shows the HRTEM images taken along [001] zone axis from the local regions in Fig. 3(a) within the dislocation cell on the left side, the track-track MPB, and the local region between the cellular boundaries on the right side, respectively. Fig. 4(a)-(c) shows the corresponding diffraction patterns taken from the local regions above using the selected-area aperture size of 1 μm. As shown in Fig. 2(b), the crystallographic orientations at both sides of the selected track-track MPB are the same with [001] zone axis. The HRTEM images shown in Figs. 4(a) and (c) display the atom columns clearly along the [001] zone axis and also indicate the same lattice parameters. Also, the diffraction patterns in Fig. 4(d) and (f) present the same microstructure information. In addition, the HRTEM and corresponding diffraction pattern of the track-track MPB, as shown in Fig. 4(b) and (e), display the same microstructure as the neighboring cellular structures, which mainly results from the specific crystallographic orientations at both sides of the selected track-track MPB and epitaxial growth characteristics at the MPB. Assuming the crystallographic orientations at both sides of the selected track-track MPB are different, the track-track MPB microstructure may seem to interface or grain boundary. As the typical microstructure features in the LPBF processed metallic materials, the role of the MPB and its contribution to the material properties need more analysis.

In metal AM, MPB is the interface that arises between the freshly solidified melt pool and the existing solid material it was built on during one melting pass [24]. Solidification typically starts at the region near the MPB with the largest thermal gradient and lowest solidification rate and towards the up center of the melt pool with a higher cooling rate [25]. Solute transport during rapid and repeated thermal cycle in AM leads to non-equilibrium solidification and non-uniform microstructures [26]. Solidification is a highly non-equilibrium process governed by the kinetics of diffusion and direction-dependent growth kinetics [27]. Classic Scheil calculation is helpful to predict the extreme case of solute segregation during the solidification process based on the classic Scheil-Gulliver model and following the assumptions of infinitely fast solute diffusion in the liquid, no solute diffusion in the solid, and thermodynamic equilibrium at the liquid/solid interface [28]. Solute diffusion in the solid (also known as back diffusion) often occurs during solidification, effectively reducing solute concentration gradients in the solid and segregation to the liquid. The Scheil with back diffusion in primary phase model solves for diffusion kinetics in the primary solid phase throughout the solidification phase, following the additional diffusion assumption considered in the primary solid phase. Furthermore, carbon is one of the most important alloying elements in steels and dissolves interstitially with high-speed diffusion rates. Carbon back diffusion plays a significant role in the solidification of steels [29]. Therefore, we defined carbon as a fast diffuser in the classic Scheil and Scheil with back diffusion in primary phase models. In addition, according to the fast cooling and undercooling of the melt in AM, austenite forms directly during the solidification without the formation of delta ferrite. The version of the ThermoCalc used in this study doesn't involve the Scheil with delta ferrite to austenite transformation model and without enabling the decomposition of ferrite, so the BCC_A2 phase was unselected in the system definer. For the Scheil-Gulliver simulation, the FCC_A1 phase is thus assumed to be the primary solidification phase.

Fig. 5(a) shows the non-equilibrium solidification paths precipitated by the Scheil-Gulliver models compared to the equilibrium path. The prediction of the non-equilibrium solidification paths presents similar fractions of solid versus temperature curves using the classic Scheil with fast diffuser model and Scheil with back diffusion in the primary phase and fast diffuser model for different cooling rates of 0.7 K/s, 10 K/s, 10^3 K/s, 10^5 K/s, 10^7 K/s. The cooling rates display apparent differences in the non-equilibrium solidification paths during the last stage of solidification when the most segregated liquid solidifies, as shown in the inset figure in Fig. 5(a). The solid fraction curve of the classic Scheil with fast diffuser simulation lay slightly below the curves of the Scheil with back diffusion in the primary phase and fast diffuser simulations. This is due to the consideration of the solute diffusion in the solid phase, which is not fully accounted for in the classic Scheil with fast diffuser model. For

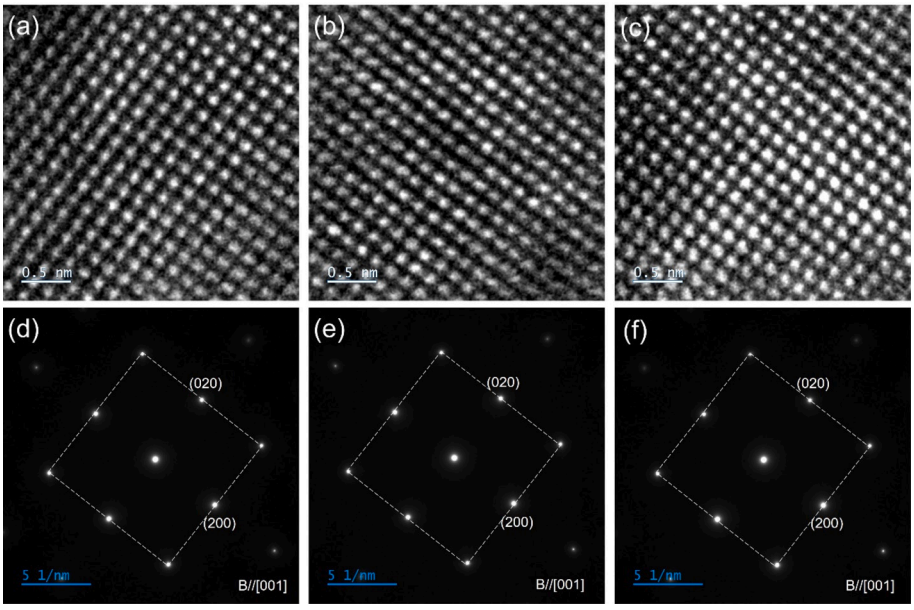

Fig. 4. (a)-(c) HRTEM images taken along [001] zone axis from the dislocation cell, MPB, and the local region between the cellular boundary, respectively, as shown in Fig. 3(a). (d)-(f) corresponding diffraction patterns taken along [001] zone axis using the selected-area aperture size of 1 μm.

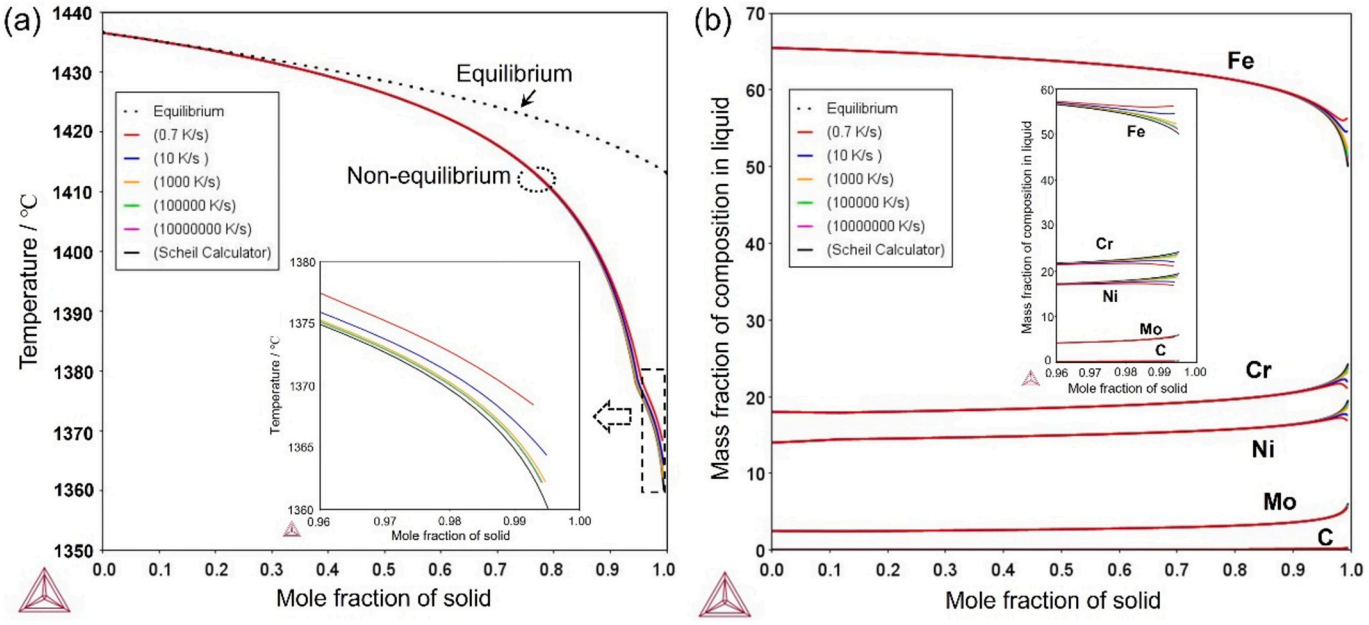

Fig. 5. Solidification simulated prediction of the equilibrium model (dotted line), classic Scheil-Gulliver with fast diffuser model (black solid line), and Scheil with back diffusion in primary phase and fast diffuser model (solid lines of red, blue, orange, green and purple indicate cooling rates of 0.7 K/s, 10 K/s, 10^3K/s, 10^5 K/s and 10^7 K/s, respectively) using the composition of 316LSS powder: (a) Temperature versus the mole fraction of solid. (b) Mass fraction of composition in liquid versus the mole fraction of solid. The inset figures show the enlarged diagram close to the end of solidification. (For interpretation of the references to colour in this figure legend, the reader is referred to the web version of this article.)

the higher cooling rates, the non-equilibrium terminates at the lower temperatures. In Fig. 5(b), the solid phase composition evolution until 99.5 % of the system is solid is shown as a function of the mass fraction of the composition in the liquid. Microsegregation patterns are qualitatively similar to the findings of the Scheil-Gulliver simulations. During the solidification process, with the increase of the mole fractions of the solid phase, the micro-segregation of all the elements gradually changes. At the first stage of solidification, there are no apparent differences in the mass fraction of composition in the liquid phase according to all the non-equilibrium Scheil simulations. At the last stage of the solidification, as shown in the insert figure indicating the slight differences at the end of the solidification, various cooling rates affecting the micro-segregation behaviors are displayed clearly. The micro-segregation profiles predicted for the higher cooling rates are comparable, whereas the lower cooling rate leads to a slower solidification process with more time for elemental back-diffusion and, thus, less severe segregations and narrow temperature ranges. The composition of Fe in the liquid decreases most significantly at the end of solidification, while Cr, Ni, and Mo elements increase slightly. A very good agreement is observed between the Scheil-Glliver predictions and STEM-EDS observations of microsegregation. However, the level of elemental micro-segregation was overestimated in the simulations compared to the experimental result.

4. Conclusion

To conclude, unique LPBF processing parameters were performed on 316LSS to control the slender columnar structures epitaxially grow from the MPB along orthogonal directions and exhibit the same growth direction across layer-layer MPB and perpendicular pattern on both sides of the track-track MPB. The exact location of the track-track MPB can be observed and identified by HAADF-STEM with the aid of the different cellular structures of the transverse and longitudinal cross-sections of columnar structures on both sides of the track-track MPB. The quantitative analysis of the segregation behavior shows that the concentration of Cr, Mo, Mn, and Ni was slightly lower, and Fe was larger by 1.5 wt% at MPB compared to the cellular interiors. The Scheil solidification simulation of the segregation behavior using ThermoCalc is in agreement with the experimental results. This study proposes a quantitative analysis method of solute segregation along the MPB, providing a deep understanding of solute segregation during the non-equilibrium solidification process. The segregation concentration can be adjusted by altering the processing conditions, further achieving microstructure manipulation by AM.

CRediT authorship contribution statement

Fei Sun: Writing – review & editing, Writing – original draft, Visualization, Validation, Supervision, Software, Resources, Project administration, Methodology, Investigation, Funding acquisition, Formal analysis, Data curation, Conceptualization. **Yoshitaka Adachi:** Supervision, Project administration, Funding acquisition. **Kazuhisa Sato:** Supervision, Data curation. **Takuya Ishimoto:** Supervision. **Takayoshi Nakano:** Supervision, Project administration, Funding acquisition. **Yuichiro Koizumi:** Supervision, Project administration, Funding acquisition.

Declaration of competing interest

The authors declare that they have no known competing financial interests or personal relationships that could have appeared to influence the work reported in this paper.

Data availability

Data will be made available on request.

Acknowledgments

This study was supported by Grant-in-Aid for Transformative Research Areas “Creation of Materials by Super Thermal Field” Research (21H05194, 21H05196, and 24H00991). This work was also partly supported by JST-CREST (Nanomechanics) (Grant Number: JPMJCR2194).

References

[1] D. Herzog, V. Seyda, E. Wycisk, C. Emmelmann, Additive manufacturing of metals, Acta Mater. 117 (2016) 371–392.

[2] M.M. Kirka, P. Nandwana, Y. Lee, R.R. Dehoff, Solidification and solid-state transformation sciences in metals additive manufacturing, Scripta Mater. 135 (2017) 130–134.

[3] D. Gu, X. Shi, R. Poprawe, D.L. Bourell, R. Setchi, J. Zhu, Material-structure-performance integrated laser-metal additive manufacturing, Science 372 (2021) eabg1487.

[4] J.H. Martin, B.D. Yahata, J.M. Hundley, J.A. Mayer, T.A. Schaedler, T.M. Pollock, 3D printing of high-strength aluminum alloys, Nature 549 (2017) 365–369.

[5] J. Ren, Y. Zhang, D. Zhao, Y. Chen, S. Guan, Y. Liu, L. Liu, S. Peng, F. Kong, J.D. Poplawsky, G. Gao, T. Voisin, K. An, Y.M. Wang, K.Y. Xie, T. Zhu, W. Chen, Strong yet ductile nanolamellar high-entropy alloys by additive manufacturing. Nature 608 (7921) 62–68.

[6] T. DebRoy, H.L. Wei, J.S. Zuback, T. Mukherjee, J.W. Elmer, J.O. Milewski, A. M. Beese, A. Wilson-Heid, A. De, W. Zhang, Additive manufacturing of metallic components–process, structure and properties, Prog. Mater. Sci. 92 (2018) 112–224.

[7] N. Ren, J. Li, R. Zhang, C. Panwisawas, M. Xia, H. Dong, J. Li, Solute trapping and non-equilibrium microstructure during rapid solidification of additive manufacturing, Nat. Commun. 14 (2023) 7990.

[8] S. Sun, T. Ishimoto, K. Hagihara, Y. Tsutsumi, T. Hanawa, T. Nakano, Excellent mechanical and corrosion properties of austenitic stainless steel with a unique crystallographic lamellar microstructure via selective laser melting, Scripta Mater. 159 (2019) 89–93.

[9] W. Abd-Elaziem, S. Elkatatny, A.-E. Abd Elaziem, M. Khedr, M.A. El-baky, M. A. Hassan, M. Abu-Okail, M. Mohammed, A. Järvenpää, T. Allam, A. Hamada, On the current research progress of metallic materials fabricated by laser powder bed fusion process: a review, J. Mater. Res. Technol. 20 (2022) 681–707.

[10] S. Chowdhury, N. Yadaiah, C. Prakash, S. Ramakrishna, S. Dixit, L.R. Gupta, D. Buddhi, Laser powder bed fusion: a state-of-the-art review of the technology, materials, properties & defects, and numerical modelling, J. Mater. Res. Technol. 20 (2022) 2109–2172.

[11] S. Kou, Welding Metallurgy, 2nd ed., John Wiley, New York, 2003.

[12] Y.B. Lei, Z.B. Wang, B. Zhang, Z.P. Luo, J. Lu, K. Lu, Enhanced mechanical properties and corrosion resistance of 316L stainless steel by pre-forming a gradient nanostructured surface layer and annealing, Acta Mater. 208 (2021) 116773.

[13] N.R. Baddoo, Stainless steel in construction: a review of research, applications, challenges and opportunities, J. Constr. Steel Res. 64 (2008) 1199–1206.

[14] Y.M. Wang, T. Voisin, J.T. McKeown, J. Ye, N.P. Calta, Z. Li, Z. Zeng, Y. Zhang, W. Chen, T.T. Roehling, R.T. Ott, M.K. Santala, P.J. Depond, M.J. Matthews, A. V. Hamza, T. Zhu, Additively manufactured hierarchical stainless steels with high strength and ductility, Nature Mater. 17 (2018) 63–71.

[15] L. Liu, Q. Ding, Y. Zhong, J. Zou, J. Wu, Y.L. Chiu, J. Li, Z. Zhang, Q. Yu, Z. Shen, Dislocation network in additive manufactured steel breaks strength–ductility trade-off, Mater. Today 21 (2018) 354–361.

[16] Z. Sun, X. Tan, S.B. Tor, C.K. Chua, Simultaneously enhanced strength and ductility for 3D-printed stainless steel 316L by selective laser melting, NPG Asia Mater. 10 (2018) 127–136.

[17] F. Sun, T. Ogawa, Y. Adachi, K. Sato, S. Takagi, G. Miyamoto, A. Suzuki, A. Yamanaka, N. Nakada, T. Ishimoto, T. Nakano, Y. Koizumi, Modulated structure formation in dislocation cells in 316L stainless steel fabricated by laser powder bed fusion, Mater. Trans. 64 (2023) 1143–1149.

[18] R.E. Kim, J. Moon, E.S. Kim, J. Lee, H.S. Kim, Surface heterostructuring of laser-clad 316L stainless steel through texture-driven deformation twinning, Scripta Mater. 221 (2022) 114989.

[19] J.J. Marattukalam, D. Karlsson, V. Pacheco, P. Beran, U. Wiklund, U. Jansson, B. Hjörvarsson, M. Sahlberg, The effect of laser scanning strategies on texture, mechanical properties, and site-specific grain orientation in selective laser melted 316L SS, Mater. Des. 193 (2020) 108852.

[20] Shifeng Wen, Shuai Li, Qingsong Wei, Yan Chunze, Sheng Zhang, Yusheng Shi, Effect of molten pool boundaries on the mechanical properties of selective laser melting parts, J. Mater. Process. Technol. 214 (2014) 2660–2667.

[21] K. Sato, S. Takagi, S. Ichikawa, T. Ishimoto, T. Nakano, Microstructure and solute segregation around the melt-pool boundary of orientation-controlled 316L austenitic stainless steel produced by laser powder bed fusion, Materials 16 (2023) 218.

[22] M. Godec, S. Zaefferer, B. Podgornic, M. Šinko, E. Tchernychova, Quantitative multiscale correlative microstructure analysis of additive manufacturing of stainless steel 316L processed by selective laser melting, Mater Charact 160 (2020) 110074.

[23] T. Ishimoto, S.Q. Wu, Y. Ito, S.H. Sun, H. Amano, T. Nakano, Crystallographic orientation control of 316L austenitic stainless steel via selective laser melting, ISIJ Inter. 60 (2020) 1758–1764.

[24] Shuai Li, Qingsong Wei, Yusehng Shi, Zicheng Zhu, Danqing Zhang, Microstructure characteristics of inconel 625 superalloy manufactured by selective laser melting, J. Mater. Sci. Technol. 31 (2015) 946–952.

[25] Y. Koizumi, M. Okugawa, Digital twin science of metal powder bed fusion additive manufacturing: a selective review of simulations for integrated computational materials engineering and science, ISIJ Int. 62 (2022) 2183–2196.

[26] Neng Ren, Ruiyao Zhang, Chinnapat Panwisawas, Mingxu Xia, Hongbiao Dong, Jianguo Li, Solute trapping and non-equilibrium microstructure during rapid solidification of additive manufacturing, Nat. Commun. 14 (2023) 7990.

[27] C. Körner, M. Markl, J.A. Koepf, Modeling and simulation of microstructure evolution for additive manufacturing of metals: a critical review, Metall. Mater. Trans. A 51 (2020) 4970–4983.

[28] Available from Thermo-calc Software, www.thermocalc.com. Accessed 7 Oct 2014.

[29] Q. Chen, B. Sundman, Computation of partial equilibrium solidification with complete interstitial and negligible substitutional solute back diffusion, Mater. Trans. 43 (2002) 551–559.